

Imaging near-surface heterogeneities with high accuracy by dispersion curves analysis and 3D elastic full-waveform inversion: which acquisition layout?

Daniela Teodor* and Cesare Comina, Univ. degli Studi di Torino; Laura Valentina Socco, Politecnico di Torino; Romain Brossier and Jean Virieux, Univ. Grenoble Alpes

Summary

We apply an integrated workflow, based on surface wave (SW) analysis and 3D elastic full-waveform inversion (FWI), to image shallow heterogeneities with high resolution. The study is focused on evaluating the effectiveness of using a 3D acquisition layout for the integrated workflow. We test various acquisition schemes with different positions of the sources with respect to a low-velocity target while evaluating the potential advantage of increasing the number of shots. All FWI tests are performed for both synthetic and field data, using various S-wave velocity (V_S) and P-wave velocity (V_P) initial models (i.e., laterally homogeneous and variable), retrieved from dispersion curves (DCs) analysis.

Introduction

The reconstruction of near-surface heterogeneities is important for evaluating the site seismic response or the accurate imaging of deeper structures (after computing the static corrections). Aside from classical methods employed for near-surface characterization, FWI, using the entire information from the seismograms, allows reaching high resolution up to half the local wavelength (Virieux and Operto, 2009). Nevertheless, FWI application on land data from shallow acquisitions is not straightforward, as such data are dominated by highly energetic and dispersive SWs. Moreover, adopting the viscoelastic equation for modeling the wave propagation may render the 3D FWI computationally oversized. To mitigate this constraint, most of the 3D time-domain FWI implementations rely nowadays on local optimization techniques. When the least-squares norm is used for the computation of the objective function, the inversion algorithm may be trapped in a local minimum if using gradient methods. Consequently, the initial model plays an important role in the convergence and the efficiency of the FWI approach. Apart from the initial model, a smart design of the acquisition scheme, prone to ensure the proper illumination of the subsurface structures, may also guide the convergence efficiently.

In this study, we use an integrated workflow, based on SW analysis and 3D elastic FWI, aimed at accurately reconstructing shallow targets, characterized by high impedance contrasts in correspondence of the boundaries. After testing various V_S and V_P initial models, retrieved by DCs analysis, with 3D FWI based on a 2D acquisition geometry (Teodor *et al.*, 2019), we investigate the effectiveness of adopting a 3D acquisition scheme for such integrated workflow. The experiments are performed for both synthetic and field data.

Methods and data sets

Our methodology for shallow targets imaging consists of integrating SW analysis with 3D elastic FWI, using the SEM46 code (Trinh *et al.*, 2019). The SW analysis relies on the method proposed by Socco *et al.* (2017) and Socco and Comina (2017), which uses an experimental relationship between the SW wavelength and the investigation depth (i.e., the W/D relationship). The W/D relationship, and its sensitivity to the Poisson's ratio variation, is employed for building initial V_S and V_P models for FWI by DC clustering and data transform (e.g., Teodor *et al.*, 2018; Khosro Anjom *et al.*, 2019). These models are integrated into a spectral element-based 3D FWI workflow.

Data sets

Both field and synthetic data sets belong to a 3D acquisition (Figure 1) containing 4 seismic lines with 18 vertical receivers each, distributed every 0.5 m. The distance between two adjacent receiver lines is 2.5 m while the sources are perpendicular to the receiver lines. The maximum offset is about 10 m. A low-velocity sand target is at the center of this acquisition layout.

The field data set belongs to a seismic acquisition performed in a test site (Khosro Anjom *et al.*, 2019). The vertical source is an 8 kg sledgehammer. For each source position, a stack of eight to ten seismograms was performed to increase the S/N. The time sampling is 0.125 ms for a total acquisition time of 0.512 s (with a pre-trig of 0.1 s).

Near-surface imaging by SW analysis and FWI

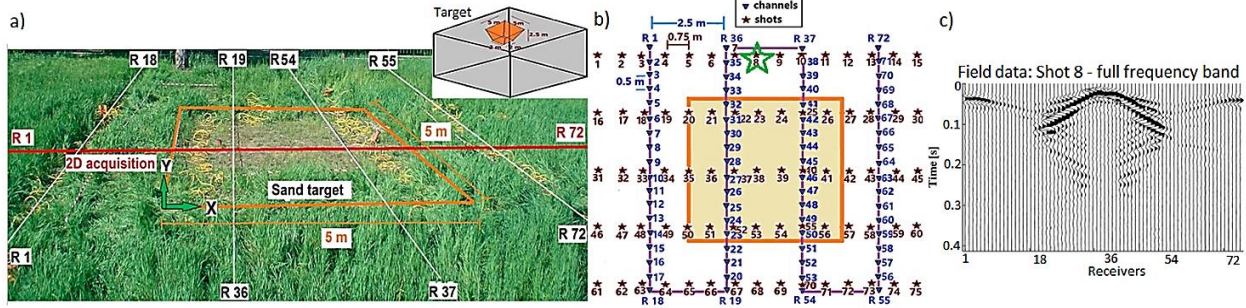


Figure 1: a) Overview of the test site and acquisition geometry. The red line R 1 – R 72 (29.3 m) indicates the receivers of the 2D acquisition (not in scale) used for DC extraction. The lines R 1 – R 18, R 19 – R 36, R 37 – R 54 and R 55 – R 72 indicate the receivers of the 3D acquisition. b) Detail of the 3D acquisition layout. c) Example of recorded data.

The synthetic data set was generated by viscoelastic wave propagation simulation through a synthetic model (Figure 2) bearing a low-velocity target that reproduces the geometry and dimensions of the real test site. The density model is homogeneous (1800 kg/m^3) while the attenuation parameters (Q_P and Q_S) are inferred by rheological relations: $Q_S = 0.15 \cdot V_S$ and $Q_P = 1.5 \cdot Q_S$ (from Hauksson and Shearer, 2006 – modified). The source is a Ricker wavelet with a central frequency of 60 Hz (similar to the field data). The forward modeling scheme is designed in agreement with the space and CFL time stability criteria: the element dimension of the 3D mesh is 0.3 m, while the time sampling is $1.4 \cdot 10^{-5}$ s, for a total duration of the simulation of 0.412 s.

Initial velocity models for FWI

We extract several DC from the recorded/simulated data using a Gaussian moving window (Bergamo *et al.*, 2012) along the seismic line R 1 – R 72. From the extracted DCs, we retrieve various initial V_S and V_P models, characterized by different lateral resolution according to the adopted workflow: Laterally homogeneous models are obtained by inverting only one DC while laterally variable models are retrieved by applying a clustering algorithm and data transform (Khosro Anjom *et al.*, 2019) to all DCs. The models are extended to 3D according to the requirements of the SEM-based FWI tool.

Parameters for 3D FWI

The FWI tests are based on the acquisition schemes displayed in Figure 3. Before FWI, we apply a 5th order Butterworth filter with corner frequencies of 3 Hz and 40 Hz and mute some noisy traces near the shots. The FWI tests are designed according to space and CFL time stability criteria: The element dimension of the 3D mesh is 1 m while the time sampling is $4.8 \cdot 10^{-5}$ s. We run all FWI tests directly in the frequency band of 3 Hz – 40 Hz and use the same sources for all iterations of each FWI experiment.

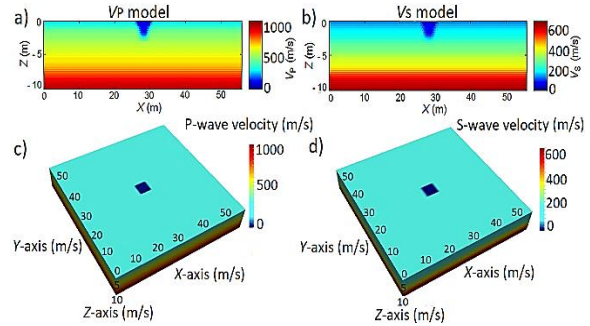


Figure 2: Synthetic (extended) model used to generate the reference (true) data set. a) and b) Vertical 2D section of the V_P and V_S model. c) and d) Detail of the shallow part of the V_P and V_S model.

For the synthetic case, we use a Ricker source while for the field data application, we estimate the field source by deconvolution (Pratt, 1999) for each experiment.

The gradient is smoothed through an anisotropic Bessel filter (Trinh *et al.*, 2017), with coherent lengths of 1.5 m, 5 m and 5 m in the z, x, and y-direction, respectively. We do not apply data normalization while we use an offset variable weighting function, to increase the contribution of the far-offset traces that bring information about the deep part of the target. The inversion scheme is based on the quasi-Newton l-BFGS method. We invert simultaneously for V_P and V_S while keeping the density (1800 kg/m^3) and the quality factors ($Q_P = Q_S = 40$) constant.

We run the FWI tests on the HPC UGA architecture using 128 cores. Each FWI test takes about 12 hours, for a maximum of 6 to 25 iterations. The FWI tests stop when the misfit function no longer decreases for more than two consecutive iterations.

Near-surface imaging by SW analysis and FWI

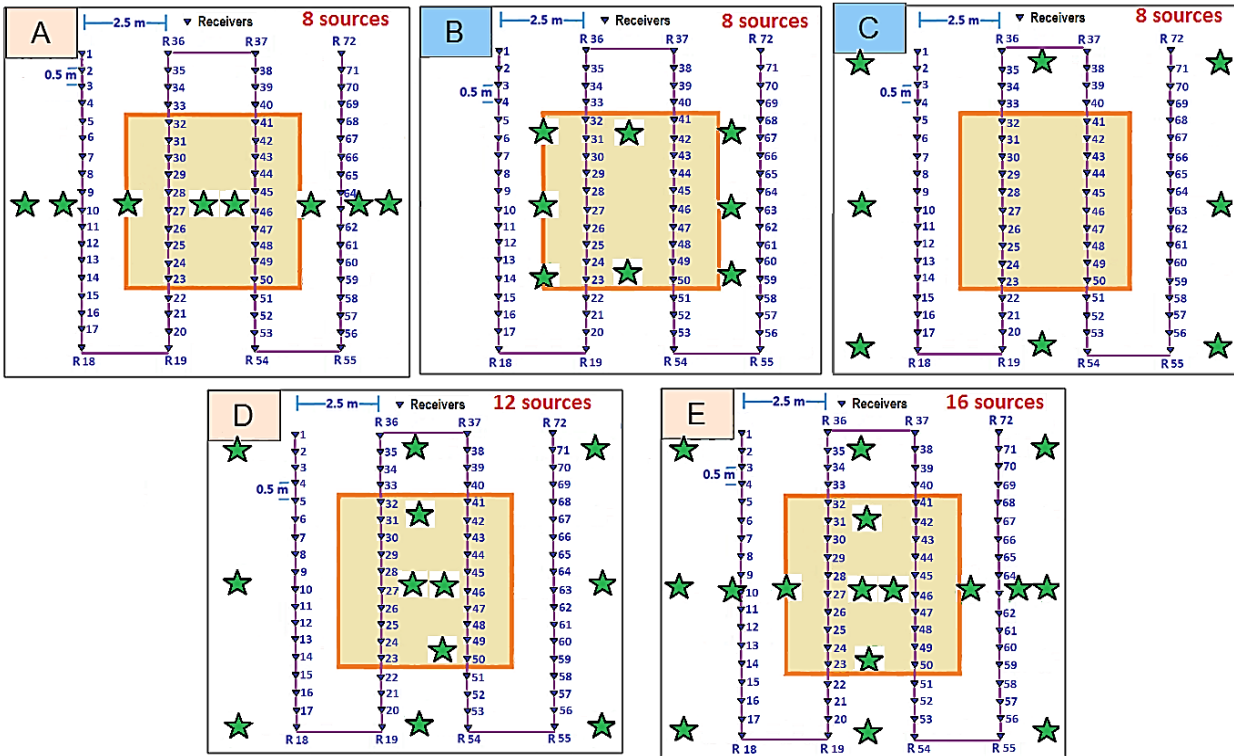


Figure 3: Acquisition layouts used for each 3D FWI experiment. The receivers are indicated with blue triangles while the sources are represented with green stars.

Results

For the acquisition schemes in Figure 3, similar results after FWI are obtained, on one side, for cases A, D and E and, on the other side, for cases B and C. Among cases A, D and E, the best results are obtained for Case E (16 shots). The lowest overall data misfit and the best V_S and V_P model reconstruction is granted by the acquisition layout of case C.

Overall, better resolution in correspondence of the target boundaries is achieved when positioning the shots outside the target (Case C) or nearby the boundaries (Case B). When positioning some sources inside the target (Case A, D and E), the estimated shallow velocity is more accurate, but the lateral extension of the target is reconstructed with lower resolution.

Figure 4a shows the evolution of the normalized data misfit during FWI for all tested cases on the synthetic data. The reader can notice that increasing the number of shots from 8 to 16 does not ensure a significantly better convergence, even if a slight decrease in the misfit occurs (green curve).

Moreover, the reader can notice that FWI results characterized by lower normalized data misfit are obtained when positioning the sources at a greater distance from the target boundaries (red curve).

As far as the initial model's effectiveness is concerned, we obtain better results when starting the FWI from laterally variable initial models (red and green curves in Figure 4b) than from laterally homogeneous ones for both synthetic experiment and field data application. The final normalized data misfit is, in these cases, 0.21 and 0.26, respectively.

Figures 5 and 6 show the results obtained when using the acquisition layout of case C and laterally variable initial models for synthetic data (Figure 5) and field data application (Figure 6). An accurate reconstruction of the target shape and lateral extension can be noticed for both synthetic and field cases. This pattern is also observed when starting the FWI from laterally homogeneous initial models. In this case, the horizontal extension of the target is precisely recovered after FWI, although few artefacts are still present in the final models.

Near-surface imaging by SW analysis and FWI

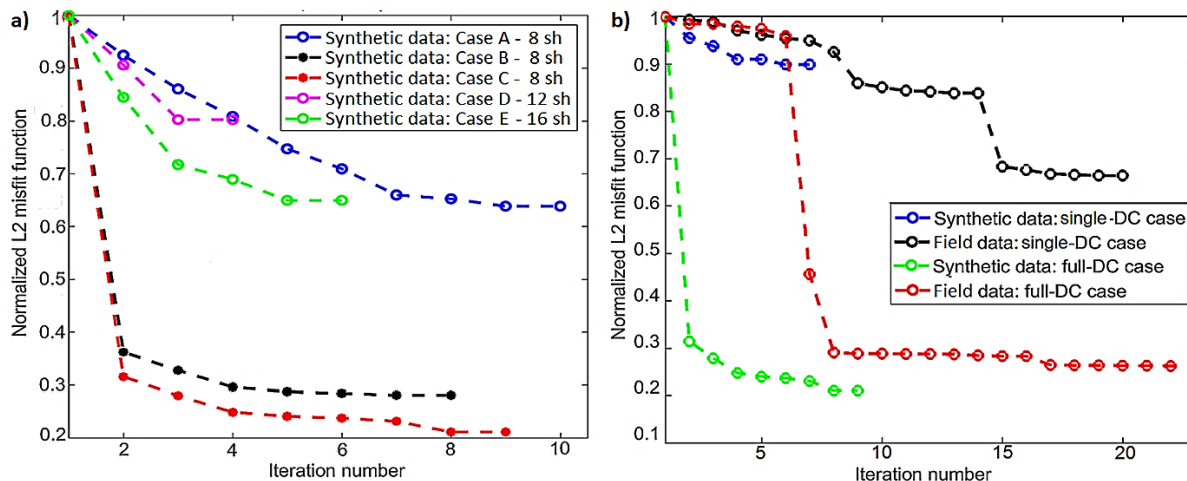


Figure 4: Normalized data misfit function a) for all synthetic tests and b) for the tests related to the Case C, synthetic and field data application, on laterally variable (full-DC) and laterally homogeneous (single-DC) initial models. For each FWI test, the misfit value of each iteration is normalized by the misfit of the first iteration.

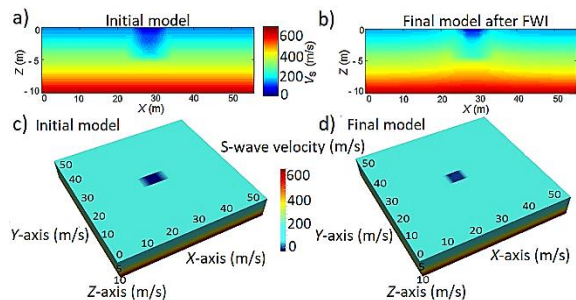


Figure 5: Synthetic results for Case C. a) 2D vertical section of the 3D initial V_S model. b) 2D vertical section of the 3D final V_S model. c) Detail of the 3D initial V_S model. d) Detail of the 3D final V_S model.

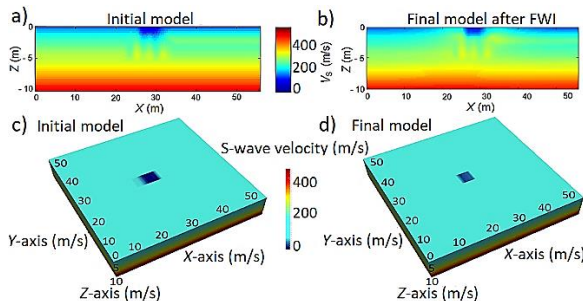


Figure 6: Results for the field data application when using the acquisition configuration of Case C. a) 2D vertical section of the 3D initial V_S model. b) 2D vertical section of the 3D final V_S model. c) Detail of the 3D initial V_S model. d) Detail of the 3D final V_S model.

Conclusions

An integrated workflow, based on the SW analysis (for the initial model building) and 3D elastic FWI, is investigated. Various FWI experiments, based on 3D acquisition layouts, provide different results, depending mainly on source positions. While increasing the number of active shots does not influence substantially the FWI results, placing the sources outside the low-velocity anomaly ensures a better reconstruction of the target boundaries and horizontal extension, as well as a significantly lower data misfit after FWI. The acquisition configuration based on sources placed at a greater distance from the low-velocity anomaly provides better results, probably because of the role played in the misfit function computation by the small-wavelength phases scattered from the target's boundaries.

Overall, when positioning some sources inside the target, despite the lower lateral resolution, a more accurate reconstruction of the shallow velocity is obtained. When placing the sources outside the target, a higher lateral resolution is achieved. Nevertheless, in this case, the shallow velocity is slightly overestimated since no source is probing the target apically.

Acknowledgements

This study was granted access to the HPC resources of CIMENT infrastructure (<https://ciment.ujf-grenoble.fr>).

REFERENCES

- Bergamo, P., D. Boiero, and L. V. Socco, 2012, Retrieving 2D structures from surface-waves data by means of space-varying windowing: *Geophysics*, **77**, no. 4, EN39–EN51, doi: <https://doi.org/10.1190/geo2012-0031.1>.
- Hauksson, E., and P. M. Shearer, 2006, Attenuation models (Q_p and Q_s) in three dimensions of the southern California crust: Inferred fluid saturation at seismogenic depths: *Journal of Geophysical Research*, **111**, B05302, doi: <https://doi.org/10.1029/2005JB003947>.
- Khosro Anjom, F., D. Teodor, C. Comina, R. Brossier, J. Virieux and L. V. Socco, 2019, Full waveform matching of V_p and V_s models from surface waves: *Geophysical Journal International*, **218**, 1873–1891, doi: <https://doi.org/10.1093/gjihttps://doi.org/ggz279>.
- Pratt, R. G., 1999, Seismic waveform inversion in the frequency domain, Part 1: Theory and verification in a physical scale model: *Geophysics*, **64**, 888–901, doi: <https://doi.org/10.1190/1.1444597>.
- Socco, L. V., and C. Comina, 2017, Time-average velocity estimation through surface-waves analysis: Part2 – S-wave velocity: *Geophysics*, **82**, no. 3, U61–U73, doi: <https://doi.org/10.1190/geo2016-0368.1>.
- Socco, L. V., C. Comina, and F. Khosro Anjom, 2017, Time-average velocity estimation through surface-waves analysis: Part1 – S-wave velocity: *Geophysics*, **82**, no. 3, U49–U59, doi: <https://doi.org/10.1190/geo2016-0367.1>.
- Teodor, D., C. Comina, F. Khosro Anjom, L. V. Socco, J. Virieux, P.-T. Trinh, and R. Brossier, 2018, Building initial models for full-waveform inversion of shallow targets by surface waves dispersion curves clustering and data transform: 88th Annual International Meeting, SEG, Expanded Abstracts, 4738–4742, doi: <https://doi.org/10.1190/segam2018-2997848.1>.
- Teodor, D., C. Comina, L. V. Socco, F. Khosro Anjom, J. Virieux, R. Brossier, and P.-T. Trinh, 2019, Elastic full waveform inversion tests for shallow targets reconstruction from surface wave analysis based initial models: 81st Conference and Exhibition, EAGE, Extended Abstracts, doi: <https://doi.org/10.3997/2214-4609.201900976>.
- Trinh, P.-T., R. Brossier, L. Métivier, L. Tvard and J. Virieux, 2019, Efficient time-domain 3D elastic and visco-elastic FWI using a spectral-element method on flexible Cartesian-based mesh: *Geophysics*, **84**, no. 1, R75–R97, doi: <https://doi.org/10.1190/geo2018-0059.1>.
- Trinh, P.-T., R. Brossier, L. Métivier, J. Virieux, and P. Wellington, 2017, Bessel smoothing filter for spectral element mesh: *Geophysical Journal International*, **209**, 1489–1512, doi: <https://doi.org/10.1093/gjihttps://doi.org/ggx103>.
- Virieux, J., and S. Operto, 2009, An overview of full-waveform inversion in exploration geophysics: *Geophysics*, **74**, no. 6, WCC1–WCC26, doi: <https://doi.org/10.1190/1.3238367>.